



Theory of direct scattering, trapping, and desorption in atom-surface collisions

Guoqing Fan¹ and J. R. Manson^{1,2,*}

¹*Department of Physics and Astronomy, Clemson University, Clemson, South Carolina 29634, USA*

²*Donostia International Physics Center (DIPC), P. Manuel de Lardizabal 4, 20018 San Sebastian, Spain*

(Received 14 July 2008; revised manuscript received 12 December 2008; published 28 January 2009)

As a part of his studies explaining how an enclosed gas comes to equilibrium, Maxwell [Philos. Trans. R. Soc. Lond. **170**, 231 (1879)] proposed what is now known as the “Maxwell assumption,” namely, that when gas particles collide with the walls of their container, a fraction is directly scattered with little change in state, while the remaining fraction becomes trapped at the surface and subsequently desorbs in a distribution at equilibrium with the surface temperature. In this paper a scattering theory is developed, using an iterative algorithm and classical mechanics for the collision process, which describes both direct scattering and trapping-desorption of the incident beam. That portion of an incident beam that is initially trapped in the physisorption potential well can be followed as the trapped atoms continue to make further interactions with the surface until they are all eventually ejected back into the continuum and leave the surface region. Several calculations show that this theory predicts when a system will obey the Maxwell assumption. Additional calculations show that the theory quantitatively explains recent experimental measurements [K. D. Gibson, N. Isa, and S. J. Sibener, *J. Chem. Phys.* **119**, 13083 (2003)] of Ar scattering from a self-assembled monolayer on Ag(111) in which clear signals of both direct scattering and a trapping-desorption fraction are exhibited in the energy-resolved spectra.

DOI: [10.1103/PhysRevB.79.045424](https://doi.org/10.1103/PhysRevB.79.045424)

PACS number(s): 34.35.+a, 68.49.Bc, 34.50.-s, 82.20.Rp

I. INTRODUCTION

Trapping and sticking are important processes that occur in gas-surface interactions. Sticking is generally associated with strong chemical bonding to the surface, and once bound the stuck particle does not desorb. Trapping, on the other hand, is associated with the physisorption potential well created by the relatively weak van der Waals potential and in many circumstances trapped gas particles will desorb after a period of residing in the well near the surface.

Maxwell,¹ in his studies of gas-surface interactions, is credited with being the first to invoke the simple assumption that a gas impinging on a surface is scattered into two fractions, one that reflects specularly and exchanges no energy and the other that equilibrates or accommodates completely and desorbs with an equilibrium distribution. This idea was taken up early in the 20th century by Knudsen,² who introduced the concept of the term “coefficient of thermal accommodation” to measure the efficiency of energy exchange at the interface between a gas and a surface and developed a theoretical framework in which to describe it. Since this early work it has become standard to assume in gas-surface collisions that the fraction of the incident gas beam that is trapped and subsequently desorbed leaves the surface in an equilibrium distribution; i.e., its accommodation coefficient is assumed to be unity and its distribution function is the Knudsen flux. This assumption of Maxwell¹ appears to be very useful because it appears to explain qualitatively experimental results measured under a wide range of different conditions. However, such an assumption has never been adequately verified theoretically.

In fact, it is clear that the first part of the Maxwell assumption, i.e., that the direct-scattering contribution is elastic, can hold strictly true only in the case of quantum-mechanical conditions, which implies low energies, small

temperatures, and small mass ratios. For classical scattering, which is the regime of large energies, high temperatures, and large mass ratios, the direct-scattering contribution leaves the surface as a distribution over a range of energies whose average is typically smaller than the energy of the incident beam, but may be larger in the case of high surface temperatures.^{3–7} However, the second part of the Maxwell assumption, i.e., that the trapping-desorption fraction leaves the surface in equilibrium, is often still today used to explain experiments.^{6,7}

The purpose of this paper is twofold. First, we test the Maxwell assumption of equilibrium for the trapping-desorption fraction using realistic calculations for a simple model of the gas-surface potential and determine when such an assumption is valid. Second, we demonstrate that a model of the interaction potential that retains the basic elements necessary for trapping, when combined with a calculation that contains correct statistical mechanics, can explain modern high-precision energy-resolved scattering measurements. The gas projectile is taken to be an atom and its interaction potential is taken to be an attractive square well with a strongly repulsive surface barrier. The calculations are carried out using classical mechanics, which is justified for many systems of interest in rarefied surface dynamics. A classical treatment means that the results will describe heavy-mass atoms at higher energies and surfaces at high temperatures where quantum-mechanical effects are not dominant. The use of an attractive square well to approximate the slowly varying van der Waals potential is also reasonable when used with a classical calculation since it gives a good description of the two primary effects upon entering the well, which are an increase in energy and a refraction of the atom to steeper angles toward the surface. The authors earlier presented results using a similar model for one-dimensional scattering.⁸ This work extends those earlier re-

sults to the much more realistic and more complicated case of fully three-dimensional scattering.⁹

Once a beam of incoming atoms interacts with the surface, a fraction will be directly scattered while the remainder will be trapped in the potential well. Of the trapped fraction, some will lose sufficient energy to be actually trapped in the well with negative total energy, while others, even though they have positive total energy, will scatter at angles sufficiently close to grazing that they will be deflected back toward the surface by the attractive part of the well. This latter positive-energy part of the trapped particles is often called the chattering fraction. The trapped portion of the incident beam particles will continue to have interactions with the surface. With each subsequent interaction some will receive enough energy and will be projected sufficiently close to the surface normal that they can escape, while the remainder will continue to be trapped. Eventually, in a closed system, all particles initially trapped will ultimately desorb from the surface, although for low temperatures and deep potential wells this could take a very large time.

For the model considered here, through an iterative algorithm, all of the trapped particles are followed as they continue to have collisions with the surface. At each iteration the negative-energy fraction, the chattering fraction, and that fraction which is desorbed are recalculated. In this manner the energy distribution of the slowly diminishing trapped particle fraction as well as the energy and angular distribution of the desorbed (or scattered) particles can be followed, and a trapping time can be calculated. By following the initial direct scattering and the sum of all the subsequently desorbed particles, the approach to equilibrium of the trapping-desorption fraction can be monitored.

What is determined is that for shallow potential wells and large surface temperatures, conditions for which little trapping is expected, the desorbed fraction leaves the surface very quickly and does not at all resemble an equilibrium Knudsen flux. However, for deeper wells and lower temperatures when the majority of the incident particles are trapped, it is found that the energy distribution of the trapped fraction rather quickly saturates to a stable functional form while the total number of trapped particles slowly diminishes. As a function of initial conditions favorable to trapping, e.g., low incident beam energy, deep wells, and low surface temperatures, the approach of the scattered particles toward an equilibrium distribution is followed. We find that in many circumstances, the energy distribution of the scattered particles readily approaches equilibrium shape even for trapping times that are relatively short. The approach of the angular distribution to equilibrium shape, which is a Knudsen cosine distribution independent of azimuthal angle, occurs more slowly and only for very large trapping times. Thus this work provides a real prediction for the conditions under which the Maxwell assumption of equilibrium for the trapping-desorption fraction can be applied with reasonable accuracy.

However, the mere fact that these calculations can indicate the conditions under which the trapping-desorption fraction may appear as a nearly equilibrium distribution is not sufficient to demonstrate that such conditions are realistic. In order to be convincing, calculations with the same potential model should be capable of explaining real experimental

measurements. To demonstrate this ability, we have chosen to compare our calculations with recent high-precision energy-resolved data for the scattering of Ar atoms from a well-ordered monolayer of the polymer 1-decanethiol adsorbed on Au(001).⁶ This experiment showed that for well-defined beams of Ar incident over a large range of energies and angles, the scattered distributions could be described by a combination of two features, a direct-scattering fraction and a trapping-desorption fraction that was nearly in equilibrium with the surface. Our calculations provide an excellent description of both contributions of the scattered spectra and produce an estimate of the average physisorption well depth of the interaction potential.

In the remainder of this paper the theory is fully developed together with a description of the iteration method in Sec. II. In Sec. III, a number of calculated results describing the approach of the trapping-desorption fraction toward equilibrium are shown and discussed. In Sec. IV, calculations are compared with the experimental data of Ref. 6. Conclusions are discussed in Sec. V.

II. THEORY

A convenient way of describing a surface scattering event is through a differential reflection coefficient, written as $dR(\mathbf{p}_f, \mathbf{p}_i)/dE_f d\Omega_f$, which gives the fraction of an incident beam of momentum \mathbf{p}_i that is scattered into the small energy interval and small solid angle in the direction of the scattered momentum \mathbf{p}_f . The differential reflection coefficient obeys the unitarity condition which assures that the number of particles scattered equals the number incident on the surface,

$$\int_0^\infty dE_f \int d\Omega_f \frac{dR(\mathbf{p}_f, \mathbf{p}_i)}{dE_f d\Omega_f} = 1. \quad (1)$$

The interaction potential is specified by a vibrating repulsive wall with a square physisorption well in front of depth D and width b , where the actual length of b plays a role in calculating the trapping times but is unimportant for all other calculations as long as it is larger than the selvage region containing the vibrational corrugations of the repulsive potential. It is assumed that the exchange of energy and momentum with the surface occurs only in collisions with the repulsive wall, while all trapped particles collide with a stationary wall at the front of the well positioned at $z=b$ that simply reflects specularly. This means that for the purpose of calculating the resulting distribution after a collision, the differential reflection coefficient is calculated using momenta that include the well depth in the normal component. For example, a particle that would have momentum \mathbf{p}_q outside the well has the momentum \mathbf{p}'_q inside where the two differ in that the energy associated with perpendicular motion is increased by the well depth,

$$p'^2_{qz} = p^2_{qz} + 2mD, \quad (2)$$

where m is the atom's mass. Similarly, an atom incident from asymptotically far away with polar angle θ_i with respect to the surface normal will be refracted inside the well into the angle

$$\cos \theta'_i = \sqrt{\frac{E_i \cos^2 \theta_i + D}{E_i + D}}. \quad (3)$$

The relationship between the differential reflection coefficients inside and outside of the well for the fraction which escapes is given by a simple Jacobian that is calculated from Eqs. (2) and (3).

Within this model, the trajectory of a given atom consists of successive collisions with the surface. The incoming beam first enters the well and then proceeds to have a first collision with the repulsive wall that scatters it into a distribution of energies and angles dictated by the differential reflection coefficient. Some of these scattered particles have sufficient energy and small enough polar angles to escape out of the well; this is the direct-scattering portion. The remaining particles are trapped, they are specularly reflected by the front face of the potential well, and then they travel back to the repulsive potential where they suffer a second collision. This process repeats multiple times until all of the initially trapped atoms eventually escape the confines of the potential well.

Based on a zeroth-order differential reflection coefficient $dR^0(\mathbf{p}_f, \mathbf{p}_i)/dE_f d\Omega_f$, which, for each collision with the repulsive potential, gives the probability of scattering from momentum state \mathbf{p}_i to \mathbf{p}_f , the total differential reflection coefficient after n such collisions can be written schematically as

$$\begin{aligned} \frac{dR^n(\mathbf{p}_f, \mathbf{p}_i)}{dE_f d\Omega_f} &= \frac{dR^0(\mathbf{p}_f, \mathbf{p}_i)}{dE_f d\Omega_f} + \int dE_b d\Omega_b \frac{dR^0(\mathbf{p}_f, \mathbf{p}_b)}{dE_f d\Omega_f} \frac{dR^0(\mathbf{p}_b, \mathbf{p}_i)}{dE_b d\Omega_b} \\ &+ \int dE_b d\Omega_b \frac{dR^0(\mathbf{p}_f, \mathbf{p}_b)}{dE_f d\Omega_f} \frac{dR^1(\mathbf{p}_b, \mathbf{p}_i)}{dE_b d\Omega_b} + \dots \\ &+ \int dE_b d\Omega_b \frac{dR^0(\mathbf{p}_f, \mathbf{p}_b)}{dE_f d\Omega_f} \frac{dR^{n-1}(\mathbf{p}_b, \mathbf{p}_i)}{dE_b d\Omega_b}, \quad (4) \end{aligned}$$

where the intermediate integrations in the higher-order terms are carried out only over those energies and angles that pertain to particles trapped in the bound states.

Such a procedure lends itself to an iterative formulation in which the scattered distribution remaining in the well after the last collision becomes the source for the next collision. The angular and energy space within the well is divided into bins sufficiently small so as to obtain good numerical precision. It is necessary to keep track separately of the three different types of trajectories, i.e., the trapped particles with negative total energy (the trapping fraction), the trapped particles with positive energy (the chattering fraction), and those that escape at each iteration (the trapping-desorption fraction).

An explicit mathematical description of how this is accomplished follows. After the n th ($n \geq 1$) iteration, the differential reflection coefficient inside the potential well $dR^n(\mathbf{p}'_f, \mathbf{p}'_i)/dE'_f d\Omega'_f$ is

$$\frac{dR^n(\mathbf{p}'_f, \mathbf{p}'_i)}{dE'_f d\Omega'_f} = \begin{cases} \frac{dR^{n-1}(\mathbf{p}'_f, \mathbf{p}'_i)}{dE'_f d\Omega'_f} + \frac{dR^n_{\text{Con}}(\mathbf{p}'_f, \mathbf{p}'_i)}{dE'_f d\Omega'_f} & \text{for } E'_f > D, \quad 0 < \theta'_f < \theta'_{fc} \\ \frac{dP^n(\mathbf{p}'_f, \mathbf{p}'_i)}{dE'_f d\Omega'_f} & \text{otherwise,} \end{cases} \quad (5)$$

where the upper line of the right-hand side of Eq. (5), labeled with the conditions $E'_f > D$ and $0 < \theta'_f < \theta'_{fc}$, gives the intensity scattered into the continuum states after n iterations and consists of the contribution that was already in the continuum state after $n-1$ iterations plus the fraction contributed to the continuum by the n th iteration. The critical angle for reflection of particles in the positive-energy chattering fraction from the front of the well is θ'_{fc} , which is dependent on energy and given by an equation similar to Eq. (3). The fraction that remains trapped in the well is divided into the sum of the positive-energy chattering fraction and the negative-energy trapped fraction, denoted by the subscripts C and T , respectively, according to

$$\frac{dP^n(\mathbf{p}'_f, \mathbf{p}'_i)}{dE'_f d\Omega'_f} = \frac{dR^n_C(\mathbf{p}'_f, \mathbf{p}'_i)}{dE'_f d\Omega'_f} + \frac{dR^n_T(\mathbf{p}'_f, \mathbf{p}'_i)}{dE'_f d\Omega'_f}. \quad (6)$$

The positive-energy chattering and negative-energy trapped fractions are further divided as follows:

$$\begin{aligned} \frac{dR^n_C(\mathbf{p}'_f, \mathbf{p}'_i)}{dE'_f d\Omega'_f} &= \left\{ [1 - N(\mathbf{p}'_f; \theta'_f)] \frac{dR^{n-1}_C(\mathbf{p}'_f, \mathbf{p}'_i)}{dE'_f d\Omega'_f} \right. \\ &\quad \left. + \frac{dR^n_{IC(C)}(\mathbf{p}'_f, \mathbf{p}'_i)}{dE'_f d\Omega'_f} + \frac{dR^n_{IT(C)}(\mathbf{p}'_f, \mathbf{p}'_i)}{dE'_f d\Omega'_f} \right\} \frac{1}{\mathcal{N}^n}, \quad (7) \end{aligned}$$

and

$$\begin{aligned} \frac{dR^n_T(\mathbf{p}'_f, \mathbf{p}'_i)}{dE'_f d\Omega'_f} &= \left\{ [1 - N(\mathbf{p}'_f; \theta'_f)] \frac{dR^{n-1}_T(\mathbf{p}'_f, \mathbf{p}'_i)}{dE'_f d\Omega'_f} \right. \\ &\quad \left. + \frac{dR^n_{IC(T)}(\mathbf{p}'_f, \mathbf{p}'_i)}{dE'_f d\Omega'_f} + \frac{dR^n_{IT(T)}(\mathbf{p}'_f, \mathbf{p}'_i)}{dE'_f d\Omega'_f} \right\} \frac{1}{\mathcal{N}^n}. \quad (8) \end{aligned}$$

In the above equations the factor $[1 - N(\mathbf{p}'_f; \theta'_f)]$, where $N(\mathbf{p}'_f; \theta'_f)$ is the ratio of normal velocity to that of the maximum normal velocity of all bound states, is given by

$$N(\mathbf{p}; \theta) = \frac{p \cos \theta}{P_z^{\text{Max}}}, \quad (9)$$

where P_z^{Max} is the largest normal momentum component of all the trapped particles and $p \cos \theta$ is the momentum component in the z direction for any other trapped particle. The terms multiplied by this factor takes account of the fact that the slower particles collide less often than the faster particles. The N^n is a normalization coefficient chosen such that $dR^n(\mathbf{p}'_f, \mathbf{p}'_i)/dE'_f d\Omega'_f$ is normalized as in Eq. (1). The intermediate differential reflection coefficients for the chattering and negative-energy trapped fractions at each iteration are given by

$$\begin{aligned} \frac{dR^n_{IC(X)}(\mathbf{p}'_f, \mathbf{p}'_i)}{dE'_f d\Omega'_f} &= \int_D dE''_q \int_{\theta'_{fc}}^{\pi/2} d\theta''_q \int_0^{2\pi} d\phi''_q \frac{dR^0(\mathbf{p}'_f, \mathbf{p}''_q)}{dE'_f d\Omega'_f} \\ &\times N(\mathbf{p}''_q; \theta''_q) \frac{dR_C^{n-1}(\mathbf{p}''_q, \mathbf{p}'_i)}{dE''_q d\Omega''_q}, \end{aligned} \quad (10)$$

and

$$\begin{aligned} \frac{dR^n_{IT(X)}(\mathbf{p}'_f, \mathbf{p}'_i)}{dE'_f d\Omega'_f} &= \int_0^D dE''_q \int_0^{\pi/2} d\theta''_q \int_0^{2\pi} d\phi''_q \frac{dR^0(\mathbf{p}'_f, \mathbf{p}''_q)}{dE'_f d\Omega'_f} \\ &\times N(\mathbf{p}''_q; \theta''_q) \frac{dR_T^{n-1}(\mathbf{p}''_q, \mathbf{p}'_i)}{dE''_q d\Omega''_q}, \end{aligned} \quad (11)$$

where the symbol X can stand for any one of the three possibilities: C for the chattering fraction, T for the negative-energy trapped fraction, or Con for the fraction that goes into the continuum. For example, $dR^n_{IT(C)}(\mathbf{p}'_f, \mathbf{p}'_i)/dE'_f d\Omega'_f$ is the intermediate differential reflection coefficient giving the probability during the n th iteration that a particle will make a transition from the negative-energy trapped fraction to the chattering fraction. Finally, the contribution to the continuum states in the total differential reflection coefficient of Eq. (5) coming from the n th iteration is

$$\frac{dR^n_{\text{Con}}(\mathbf{p}'_f, \mathbf{p}'_i)}{dE'_f d\Omega'_f} = \frac{1}{N^n} \frac{dR^n_{IC(\text{Con})}(\mathbf{p}'_f, \mathbf{p}'_i)}{dE'_f d\Omega'_f} + \frac{1}{N^n} \frac{dR^n_{IT(\text{Con})}(\mathbf{p}'_f, \mathbf{p}'_i)}{dE'_f d\Omega'_f}. \quad (12)$$

At the end of n iterations the fraction of all incident particles that remain trapped in the positive-energy chattering states is

$$P_C^n = \int_D dE'_f \int_{\theta'_{fc}}^{\pi/2} d\theta'_f \int_0^{2\pi} d\phi'_f \frac{dP_C^n(\mathbf{p}'_f, \mathbf{p}'_i)}{dE'_f d\Omega'_f}, \quad (13)$$

while the fraction trapped with negative total energies is

$$P_T^n = \int_0^D dE'_f \int_0^{\pi/2} d\theta'_f \int_0^{2\pi} d\phi'_f \frac{dP_T^n(\mathbf{p}'_f, \mathbf{p}'_i)}{dE'_f d\Omega'_f}. \quad (14)$$

Thus the total trapped fraction after n iterations is

$$P^n = P_C^n + P_T^n. \quad (15)$$

The fraction escaping into the continuum state after n iterations is

$$P_{\text{Con}}^n = \int_D dE'_f \int_0^{\theta'_{fc}} d\theta'_f \int_0^{2\pi} d\phi'_f \frac{dR^n(\mathbf{p}'_f, \mathbf{p}'_i)}{dE'_f d\Omega'_f}, \quad (16)$$

and the unitarity condition assures that the total number of particles is conserved,

$$P_C^n + P_T^n + P_{\text{Con}}^n = 1. \quad (17)$$

The major numerical operations in this procedure are the two volume integrals associated with evaluation of the intermediate differential reflection coefficients of Eqs. (10) and (11) and the unitarity summations of Eqs. (13), (14), and (16), which taken together amount to a six-dimensional integral. The angular integrations are carried out using Gauss-Legendre quadratures and the energy integrals use Gauss-Laguerre quadratures. Because classical differential reflection coefficients are positive definite and typically tend to consist of a single broad peak or a small number of such peaks in both the energy and angular variables, Gauss quadratures are ideally suited for these integrals.

The only remaining element of this procedure that needs to be specified is the zeroth-order differential reflection coefficient. There are a number of choices that have been used in the past to describe classical mechanical collisions of atoms with vibrating surfaces.¹⁰⁻¹² The simplest of these, and the most appropriate for the present calculations, is the differential reflection coefficient for an atomic projectile colliding with a surface of discrete scattering centers of mass M whose initial momenta are distributed in an equilibrium distribution at temperature T_S . This is given by¹²⁻¹⁴

$$\begin{aligned} \frac{dR^0(\mathbf{p}_f, \mathbf{p}_i)}{dE_f d\Omega_f} &= \frac{m^2 |\mathbf{p}_f|}{8\pi^3 \hbar^4 p_{iz}} |\tau_{fi}|^2 \left(\frac{\pi}{k_B T_S \Delta E_0} \right)^{1/2} \\ &\times \exp \left\{ - \frac{(E_f - E_i + \Delta E_0)^2}{4k_B T_S \Delta E_0} \right\}, \end{aligned} \quad (18)$$

where $\Delta E_0 = (\mathbf{p}_f - \mathbf{p}_i)^2 / 2M$ is the recoil energy, p_{iz} is the z component of the incident momentum, k_B is the Boltzmann constant, and $|\tau_{fi}|^2$ is the form factor of the scattering center which depends on the interaction potential. To lowest order, the amplitude τ_{fi} is identified as the transition matrix element of the elastic interaction potential extended off the energy shell.¹⁵ However, for this work we use the value appropriate for hard sphere scattering which is a constant. The differential reflection coefficient of Eq. (18) can be obtained from a purely classical calculation or from a quantum-mechanical formulation in which the classical limit is extracted. In the case of a completely classical derivation, the constant \hbar is unspecified except for its dimensions of action, whereas quantum derivations identify \hbar as Planck's constant divided by 2π .

To obtain the trapping time τ a variety of methods can be used, but we have found that the most convenient is to first calculate the average speed normal to the surface for the trapped particles after each iteration. The time for that iteration is then determined as that required to travel the distance $2b$ from the repulsive wall to the front of the well and back.

The average normal speed for the positive-energy trapped fraction is

$$\langle v_n \rangle_C = \frac{1}{P_C^n} \int_D dE'_f \int_{\theta'_f}^{\pi/2} d\theta'_f \int_0^{2\pi} d\phi'_f \sqrt{\frac{2E'_f}{m}} \times \cos(\theta'_f) \frac{dP_T^n(\mathbf{p}'_f, \mathbf{p}'_i)}{dE'_f d\Omega'_f}, \quad (19)$$

and for the negative-energy trapped fraction it is

$$\langle v_n \rangle_T = \frac{1}{P_T^n} \int_0^D dE'_f \int_0^{\pi/2} d\theta'_f \int_0^{2\pi} d\phi'_f \sqrt{\frac{2E'_f}{m}} \times \cos(\theta'_f) \frac{dP_T^n(\mathbf{p}'_f, \mathbf{p}'_i)}{dE'_f d\Omega'_f}. \quad (20)$$

The total trapping time is then given by summing the times at each iteration,

$$\tau = 2b \sum_n \left(\frac{1}{\langle v \rangle_T} \frac{P_T^n}{P^0} + \frac{1}{\langle v \rangle_C} \frac{P_C^n}{P^0} \right) = \tau_T + \tau_C, \quad (21)$$

where P^0 is the fraction of initially trapped particles. The actual definition of trapping time used in this work is the time required for the fraction of trapped particles remaining in the well to be reduced to 1% of the number of incident atoms.

The method of calculation of the average trapping time is clearly not unique, and we have evaluated it several ways using the trapped fraction probabilities as in Eqs. (19) and (20) above. For example, instead of determining the average speed, one can use the root-mean-square normal speed, or find the average time directly by obtaining the average of $2b/v_z$ at each iteration. In cases in which the trapping time is relatively long, all of these different methods yielded values which were quite similar. For all average trapping times reported here the width of the well was taken to be $b=3\text{\AA}$, and Eq. (21) shows that τ scales linearly with b .

III. APPROACH TO EQUILIBRIUM

In this section we present a number of calculations that demonstrate the approach toward an equilibrium distribution of the trapping-desorption fraction. The parameters are primarily chosen to represent monoenergetic and angularly defined beams of either Ar or Ne scattering from a tungsten surface. This leads to a set of guidelines for when one may expect the Maxwell assumption to be valid, i.e., for when the trapping-desorption fraction approximates an equilibrium distribution.

Figure 1 shows an example calculation of the evolution of the energy distribution as a function of number of iterations for the case of argon scattering from a tungsten surface. The incident angle is 45° , the incident energy is 1 meV, the well depth is chosen to be 80 meV, and the surface temperature is 273 K. The dotted curve shows the continuum energy distribution after the first iteration, which is the second collision with the surface. The trapping fraction is $P^1=0.953$, indicating that 95.3% of the incident particles remain trapped in the potential well. The dashed and dash-dotted curves show the evolution of the continuum scattered distribution after in-

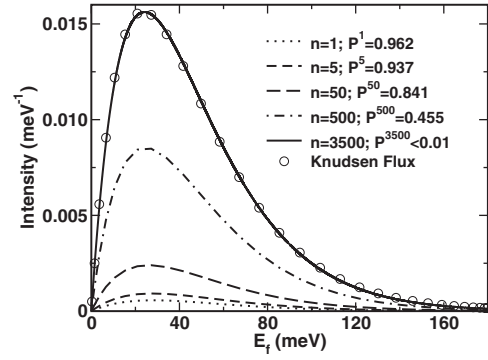


FIG. 1. Argon scattering from a tungsten surface: the evolution of the final energy distribution for particles scattered into the continuum states after a specified number of iterations. The surface temperature is 273 K, the incident energy $E_i=1$ meV, the well depth D is 80 meV, and the incident angle $\theta_i=45^\circ$. Five curves of the final distributions for the iteration numbers $N=1, 5, 50, 500,$ and 3500 are shown. For comparison a Knudsen equilibrium flux is given as open circles.

creasing numbers of iterations of 5, 50, and 500. After 500 iterations there is still approximately one-third of the incident particles trapped. After 3500 iterations the trapped fraction drops below the arbitrary threshold of 1% of the incident particles.

Also shown for comparison in Fig. 1 is the Knudsen distribution given by

$$\frac{dK}{dE_f d\Omega_f} = \frac{E_f \cos \theta_f}{\pi (k_B T_G)^2} \exp \left\{ -\frac{E_f}{k_B T_S} \right\}. \quad (22)$$

It is clearly seen that the total scattered distribution closely approximates the Knudsen flux when nearly all the initially trapped particles have been desorbed.

What is actually plotted in Fig. 1 is the integral over all final angles of the differential reflection coefficient, which is essentially the average energy distribution scattered over all outgoing angles. However, the energy distribution at any fixed final polar and azimuthal angle behaves quite similarly, and at the maximum iteration number the dependence of the distribution on energy is essentially the same at all angles. This is in agreement with the Knudsen flux which has exactly the same energy dependence at all final angles.

The average trapping time as calculated using the average normal speed from Eq. (19) in order to reach the arbitrary threshold of 1% of the particles still remaining trapped is $\tau \approx 6.71 \times 10^{-9}$ s. If the number of iterations is extended to larger than the $N=3500$ shown in Fig. 1, there is essentially no change in the scattered distribution because the number of particles remaining in the well is insignificant.

For incident energies small compared to the well depth D , the final, converged energy distribution after a large number of iterations is independent of incident energy and incident angle. However, the distributions calculated after only a small number of iterations will vary somewhat with the choice of these incident parameters.

The evolution of the angular distribution for the same Ar/W system as shown in Fig. 1 except for a higher tempera-

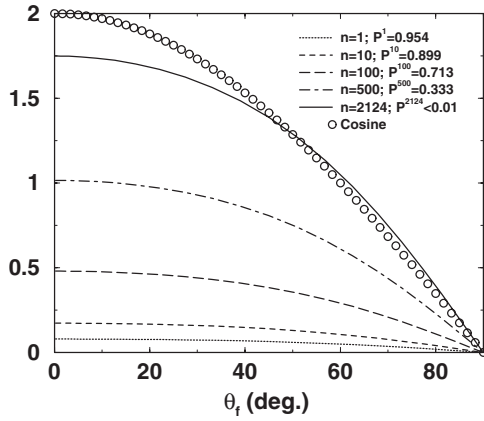


FIG. 2. The evolution of the final distribution in polar angle θ_f for the Ar/W system with the same parameters as in Fig. 1 except that the temperature is 303 K. A Knudsen cosine distribution is shown as open circles.

ture $T_S=303$ K is given in Fig. 2. It is seen that as the number of iterations increases, the angular distribution as a function of the polar angle θ_f gradually approaches the cos θ_f form of the Knudsen flux, which is shown as open circles. The calculations of Figs. 1 and 2 very quickly become independent of the azimuthal angle ϕ even for very small numbers of iterations. This is consistent with the behavior of the Knudsen flux which is independent of azimuthal angle.

For the set of initial conditions chosen in Fig. 2, it is seen that the angular distribution does not achieve a Knudsen distribution even at the largest iteration number calculated. The shape closely resembles a cosine function but, for example, its value at $\theta_f=0$ is only about 88% of that for the corresponding Knudsen cosine. This behavior is typical of many of the systems examined. If the well depth is sufficiently large and the incident energy is small compared to D and $k_B T_S$, the system will usually achieve an equilibrium energy distribution after large numbers of iterations and it becomes independent of azimuthal angle very quickly. But the polar angular distribution is usually very slow to converge to the equilibrium cosine distribution as seen in Fig. 2 and also in Fig. 4.

The evolution of a system toward a final equilibrium distribution as a function of potential-well depth D is shown in Fig. 3. The parameters are similar to the Ar/W system of Fig. 1 and the projectile is incident normally at $\theta_i=0^\circ$ with $E_i=1$ meV and $T_S=273$ K, but completely converged calculations (meaning less than 1% of the incident particles remain trapped) are shown for the three different well depths of 20, 50, and 80 meV. This figure shows clearly that even if the incident energy is very small and the initially trapped fraction is large, the total scattered distribution does not approach equilibrium unless the adsorption well is sufficiently deep to cause long average trapping times. For a shallow well of 20 meV with an average desorption time of about 5.3×10^{-10} s as shown in Table I the final distribution deviates strongly from an equilibrium distribution. It is only when the well depth is increased to about 80 meV that near-equilibrium conditions are achieved.

The response of the angular distribution of the final scattered particles for the same conditions as shown in Fig. 3 is

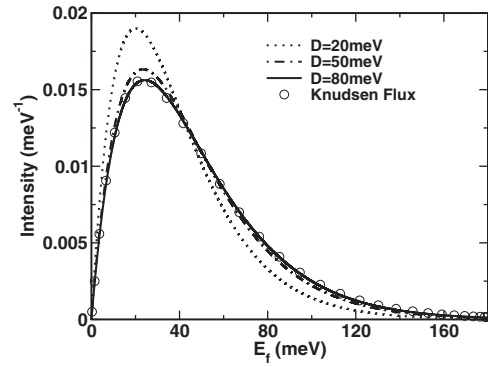


FIG. 3. Final energy distributions for the Ar/W system as a function of potential-well depths $D=20, 50,$ and 80 meV are shown. The temperature of the surface is 273 K, the incident energy $E_i=1$ meV, and $\theta_i=0^\circ$. A Knudsen distribution is shown as open circles.

given in Fig. 4. The progression toward a cosine distribution is clearly evident with increasing well depth, but even for the rather large value of $D=120$ meV, for which the average trapping time is 1.28×10^{-7} s, the result deviates somewhat from cosine behavior, although at $\theta_f=0^\circ$ the calculated value is 91% of the cosine maximum.

An example showing the effect of mass on the convergence toward equilibrium is shown in Fig. 5 corresponding to Ne scattering from tungsten at 1 meV of incident energy. For this system the mass ratio is roughly half that of Ar/W and approximate equilibrium behavior is not achieved unless the well depth is approximately 150–200 meV in depth. The corresponding average trapping time for $D=200$ meV is about 3.9×10^{-7} s as seen from Table II.

The effects of mass on the approach to equilibrium are even more dramatically exhibited in Fig. 6, which shows the scattered energy distribution as a function of the projectile

TABLE I. The desorption times τ and initial sticking fractions P^0 for Ar/W. E_i is 1 meV, θ_i is 45° , and T_S is 303 K, and well depths ranging from 20 to 200 meV are shown. The upper set of values was obtained from the normal rms speed of trapped particles, and the lower set of values was determined from the average normal speed.

Ar/W	τ_{rmsC}	τ_{rmsT}	τ_{rms}	P^0
$D=20$ meV	1.28×10^{-10}	1.66×10^{-10}	2.94×10^{-10}	0.825
$D=50$ meV	1.26×10^{-10}	6.63×10^{-10}	7.89×10^{-10}	0.933
$D=70$ meV	1.35×10^{-10}	1.58×10^{-9}	1.72×10^{-9}	0.958
$D=80$ meV	1.40×10^{-10}	2.42×10^{-9}	2.56×10^{-9}	0.966
$D=200$ meV	1.99×10^{-10}	3.59×10^{-7}	3.59×10^{-7}	0.995
τ (\bar{v})	τ_C	τ_T	τ	
$D=20$ meV	2.27×10^{-10}	3.04×10^{-10}	5.31×10^{-10}	
$D=50$ meV	2.10×10^{-10}	1.16×10^{-9}	1.37×10^{-9}	
$D=70$ meV	2.21×10^{-10}	2.74×10^{-9}	2.96×10^{-9}	
$D=80$ meV	2.29×10^{-10}	4.20×10^{-9}	4.43×10^{-9}	
$D=200$ meV	3.26×10^{-10}	6.40×10^{-7}	6.40×10^{-7}	

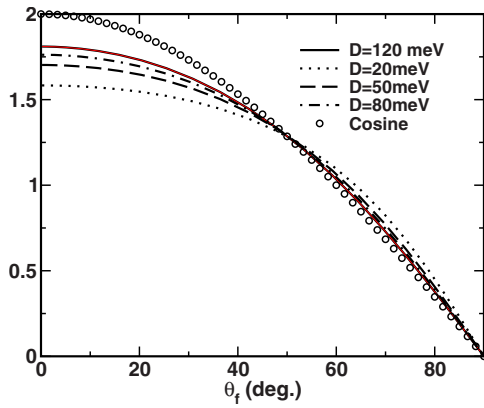


FIG. 4. (Color online) The polar angular distribution for the same system shown in Fig. 3. The evolution toward the Knudsen distribution, displayed as open circles, is shown for a series of increasing well depths.

surface mass ratio μ . The well depth is chosen to be 50 meV, the incident energy is 1 meV, $\theta_i=45^\circ$, and the temperature is 303 K. When the mass ratio is small, for instance $\mu=0.005$ corresponds to hydrogen atoms scattering from tungsten, the total scattered intensity is far from an equilibrium distribution. However, for a mass ratio of about one-half the scattered spectra is very nearly in equilibrium.

Larger temperatures tend to make initial trapping more difficult and lead to more rapid desorption. Thus at high temperatures the trapping-desorption fraction will deviate more strongly from an equilibrium distribution. This is shown in Fig. 7, where calculations are shown for similar initial conditions as in Fig. 1, i.e., Ar/W at a low incident energy of 1 meV and a well depth of 80 meV, but three different surface temperatures of 303, 600, and 1200 K. For each temperature a Knudsen flux distribution is shown as points. For the lowest temperature the scattering is in very good agreement with the corresponding Knudsen equilibrium curve, but begins to deviate quite strongly as the temperature is increased. As the temperature is increased to the point where the trapping-desorption no longer is in equilibrium, the average final energy becomes less than the $2k_B T_S$ value of the Knudsen distribution.

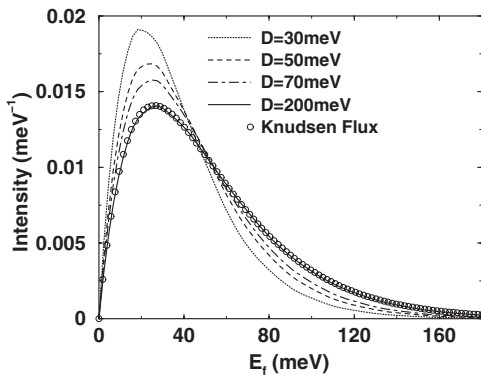


FIG. 5. Energy distributions of the scattered particles for Ne/W for several well depths are shown. The temperature of the surface is 303 K, the incident energy $E_i=1$ meV, and $\theta_i=0^\circ$. The Knudsen distribution is shown as open circles.

TABLE II. The desorption time for Ne/W with other parameters the same as in Table I.

Ne/W	τ_C	τ_T	τ	P^0
$D=20$ meV	9.56×10^{-11}	1.35×10^{-10}	2.30×10^{-10}	0.848
$D=30$ meV	9.50×10^{-11}	2.10×10^{-10}	3.05×10^{-10}	0.891
$D=70$ meV	9.47×10^{-11}	1.11×10^{-9}	1.20×10^{-9}	0.954
$D=80$ meV	9.70×10^{-11}	1.66×10^{-9}	1.76×10^{-9}	0.961
$D=150$ meV	1.16×10^{-10}	2.88×10^{-8}	2.89×10^{-8}	0.984
$D=200$ meV	1.29×10^{-10}	2.22×10^{-7}	2.22×10^{-7}	0.990

$\tau(\bar{v})$	τ_C	τ_T	τ
$D=20$ meV	1.73×10^{-10}	2.42×10^{-10}	4.16×10^{-10}
$D=30$ meV	1.59×10^{-10}	3.70×10^{-10}	5.29×10^{-10}
$D=70$ meV	1.58×10^{-10}	1.92×10^{-9}	2.07×10^{-9}
$D=80$ meV	1.61×10^{-10}	2.88×10^{-9}	3.04×10^{-9}
$D=150$ meV	1.89×10^{-10}	5.07×10^{-8}	5.08×10^{-8}
$D=200$ meV	2.10×10^{-10}	3.93×10^{-7}	3.93×10^{-7}

The method of calculation presented here permits an examination of the energy distribution of the trapped particles at any average time after the initial collision. An example of this is shown in Fig. 8 for Ar/W with the same initial conditions as in Fig. 2. Both the negative-energy trapped fraction and the positive-energy chattering fraction are exhibited. It is seen that even after a very few iterations a smooth distribution with a maximum in the negative-energy range appears. As the iteration number increases, the most probable energy of all of the trapped particles shifts downward toward the bottom of the well as the trapped particles continue to lose energy to the surface on average. For very large numbers of iterations the trapped distribution begins to look exponential-like as a function of energy and reaches a steady-state distribution that retains essentially the same functional form but gradually decreases in total integrated area as more and more particles are desorbed. Interestingly, just after the initial collision the positive-energy chattering fraction extends outward to rather large energies with nonzero amplitude at positive total energies larger than the magnitude of the well depth.

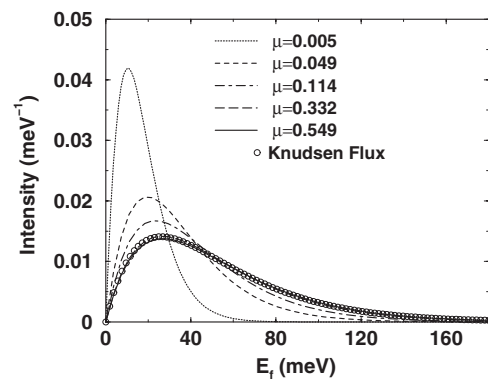


FIG. 6. The energy distribution as a function of the mass ratio μ for a system with $\theta_i=45^\circ$, $E_i=1$ meV, $T_S=303$ K, and $D=50$ meV.

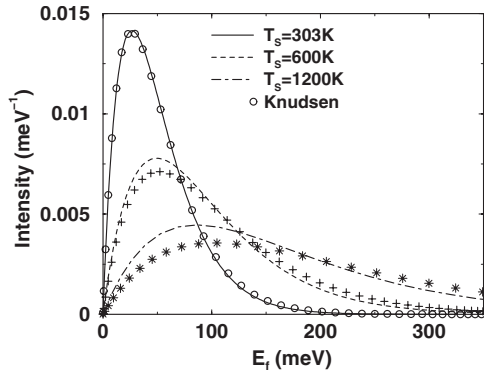


FIG. 7. Energy distribution of the scattered particles for Ar/W with incident energy $E_i=1$ meV, $\theta_i=45^\circ$, and a well depth $D=80$ meV. Three different surface temperatures $T_S=303, 600,$ and 1200 K are shown as curves. The corresponding equilibrium distributions are shown as circles, crosses, and stars, respectively.

Some representative calculations of average trapping times τ are shown in Tables I and II based on the assumption of a square well of width $b=3\text{\AA}$. Table I shows calculations for the Ar/W system of Fig. 1 with 1 meV of incident energy and $T_S=303$ K. The trapping times for several well depths are calculated in two slightly different ways, first by obtaining the average speed after each iteration as in Eqs. (19) and (20) and then also from the root-mean-square speed. The two contributions to the total τ from the negative-energy trapped fraction and from the positive-energy trapped fraction are exhibited separately. Also shown in Table I are the trapped fractions after the initial collision P^0 . Table II shows similar information calculated for the Ne/W system of Fig. 5 with the same incident energy and temperature.

For both systems the results are similar. For shallow well depths the trapping times are very short and the average times spent in negative- and positive-energy trapped states are comparable. As the well depth is increased, trapping times increase dramatically and the average time spent in the positive-energy chattering state becomes negligible compared to the average time in the negative-energy bound states. This increase in trapping times is nearly exponential as a function of well depth as seen in Fig. 9, which graphs the numbers presented in Tables I and II. Generally, the trap-

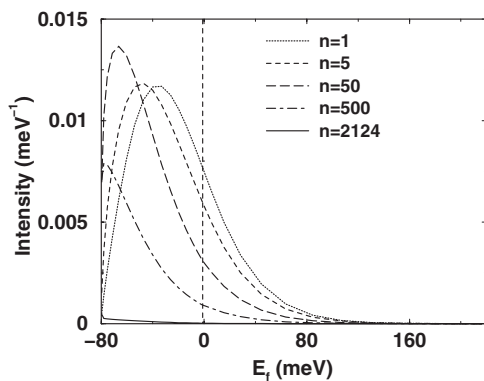


FIG. 8. The evolution of the energy distribution inside the potential well as a function of iteration number for the same system as in Fig. 2.

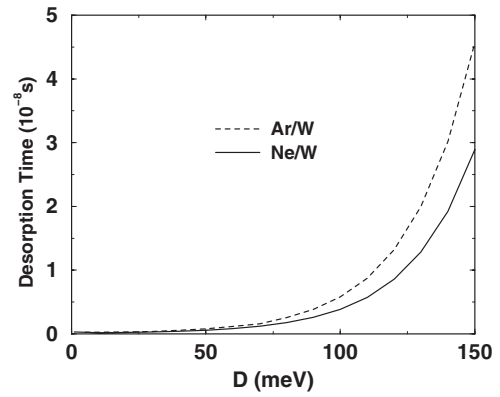


FIG. 9. The desorption times for Ar/W and Ne/W as functions of the well depth for the incident conditions shown in Tables I and II.

ping times based on the rms speed after each iteration are somewhat smaller than those based on a calculation of the average speed. For Ar/W with a physically reasonable well depth of around 100 meV, the average trapping time for 99% of the initially trapped particles to desorb is approximately 10^{-8} s.

All of the above calculations have been done for energies relatively small compared to the well depths in order to illustrate the conditions for which the trapping-desorption fraction approaches an equilibrium distribution. When the incident energy becomes comparable to or larger than the well depth, the nature of the scattered intensity becomes quite different. As noticed in an important series of experiments first performed some years ago, the intensity often exhibits a double-peaked structure, with a high-energy peak due to direct scattering and a lower-energy peak arising from the trapping-desorption fraction.³ Figure 10 shows this for a system corresponding to Ar/W with $\theta_i=45^\circ$, $D=80$ meV, $T_S=303$ K, and incident energies ranging from 100 to 500

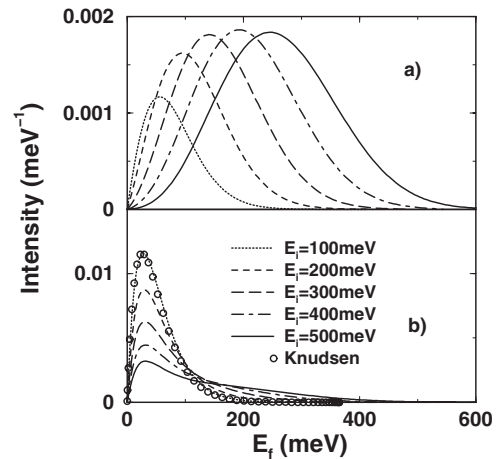


FIG. 10. The direct and trapping-desorption scattering energy distributions for incident energies that are large compared to the well depth. The system is Ar/W with $\theta_i=45^\circ$, $D=80$ meV, $T_S=303$ K, and incident energies as marked. (a) The upper panel shows the direct-scattering contribution, and (b) the lower panel shows the trapping-desorption intensity. A Knudsen distribution is also included in the lower panel.

meV as marked. The two contributions are shown in separate panels, with the upper panel giving the direct scattering and the lower panel giving the trapping-desorption. With increasing E_i the total integrated direct scattering becomes larger and the peak becomes broader, with the width roughly increasing proportionately to $\sqrt{E_i}$. For the direct scattering the energy dependence of the widths, as well as the most probable final energies, is consistent with estimates based on binary collisions as discussed below in connection with Eqs. (23)–(25).

On the other hand the total trapping-desorption fraction, shown in the lower panel, becomes smaller and with increasing incident energy the shape of the distribution becomes less and less like that of an equilibrium Knudsen curve. For large E_i the trapping-desorption intensity develops a long high-energy tail although its peak position always remains near to the most probable energy of the Knudsen distribution. The situation in which the differential reflection coefficient exhibits both distinct direct and trapping-desorption peaks is discussed further in Sec. IV in the context of comparisons of the present theoretical model with recent experimental data.

IV. COMPARISONS WITH EXPERIMENT

The calculations exhibited in Sec. III describe the range of initial conditions that lead to an equilibrium distribution in the trapping-desorption fraction, but no comparisons with experimental data other than to a Knudsen distribution were made. However, in order to be credible, the theoretical approach should be capable of explaining real experiments. Demonstrating that ability is the objective of this section.

There is a long history of gas-surface scattering experiments using hyperthermal atoms^{3,4,7,16–27} and molecules^{28–40} as projectiles. If the projectile gas has mass larger than that of hydrogen or helium, such high energies imply that the scattering will be classical, which means that many phonons will be transferred in the collision. This is the type of experiment that should be amenable to the theoretical treatment described here. In many cases the energy-resolved scattered spectra exhibit a double-peaked structure, with a somewhat narrow high-energy peak centered at smaller energy than the incident-beam energy (if the incident energy is large compared to the surface temperature) and a broader low-energy peak at thermal energies. The usual interpretation has been that the high-energy peak is direct scattering from a single collision (or at most, a very small number of collisions) and the low-energy peak arises from trapping in the physisorption well of the interaction potential with subsequent desorption at a sufficiently later time so that those particles come into near equilibrium at the surface temperature.³

A recent and important paper reporting extensive measurements that show clearly a set of conditions for which direct scattering and trapping-desorption can be observed is that of Gibson *et al.*⁶ for scattering of Ar from an ordered 1-decanethiol self-assembled overlayer on a Au(111) substrate. The experiments were carried out with well-defined monoenergetic beams of Ar incident at energies ranging from roughly 60 to 600 meV, and with both incident and detector angles independently variable and ranging from near normal

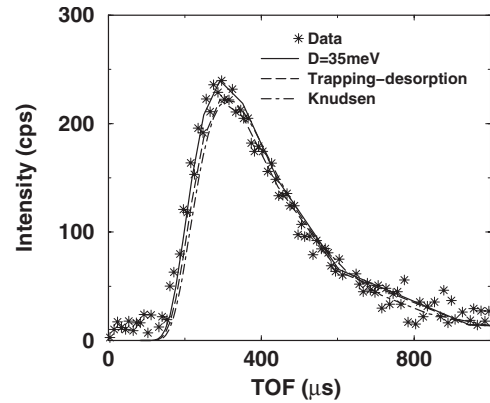


FIG. 11. Intensity versus TOF for Ar scattering from a 1-decanethiol layer on Au(111) with $E_i=65.3$ meV, $\theta_i=45^\circ$, and $\theta_f=50^\circ$. The calculation shown as a solid curve is the total differential reflection coefficient converted to TOF calculated with $\mu=0.56$ and $D=35$ meV, the dash-dotted curve is the trapping-desorption fraction, and the dotted curve is a Knudsen equilibrium distribution.

to near grazing with respect to the surface. All measurements were made in the scattering plane (the plane containing the surface normal and the incident beam), which was aligned along the $\langle 1\bar{1}0 \rangle$ direction of the Au(111) surface. At low incident energies and if θ_i or θ_f was near normal, Gibson *et al.*⁶ did not observe a clear double-peaked intensity in the scattered spectra. However, at higher energies and for large incident or final angles, the characteristic double-peaked structure was very apparent. Gibson *et al.*⁶ analyzed their data quantitatively with an *ad hoc* model consisting of the sum of a shifted Maxwell-Boltzmann distribution to fit the direct scattering and an equilibrium distribution to fit the trapping-desorption fraction. They also made some more qualitative analysis of their data using classical trajectory calculations developed by Hase *et al.*⁴¹ In the process of their analysis they determined, by assuming that the direct scattering was due to a single collision and using well-known Baule relations for binary collisions, that the effective mass of the surface implied a mass ratio $\mu=0.62$, or $M_C=64.4$ amu, as opposed to the total mass of the 1-decanethiol, which is 174.3 amu. The potential-energy landscape function developed for the classical trajectory calculations had a well depth ranging from 33 meV at the on-top sites above the terminal CH_3 groups to 67 meV in the center of the rhombus formed by a group of four of the methyl groups.⁶

Figure 11 shows an example of calculations compared to the Ar scattering data taken from the upper panel of Fig. 2 of Ref. 6, and this is for the lowest incident energy $E_i=65.3$ meV. The data were reported as intensity versus time of flight (TOF), and the calculations have been transformed accordingly. The other incident parameters are $\theta_i=45^\circ$, $\theta_f=50^\circ$, and $T_S=135$ K. The calculations were carried out for a well depth $D=35$ meV and an effective surface mass $M_C=71$ amu ($\mu=0.56$).

This effective surface mass ratio is slightly smaller than the value $\mu=0.62$ estimated in Ref. 6. For this case of low incident energy, the calculations are not particularly sensitive to the value of μ because there is very little evidence for a

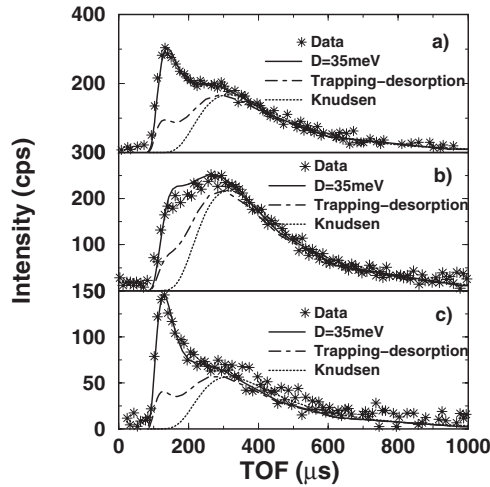


FIG. 12. Intensity versus TOF for Ar scattering from a 1-decanethiol layer on Au(111) with $E_i=365$ meV: (a) $\theta_i=45^\circ$ and $\theta_f=50^\circ$, (b) $\theta_i=30^\circ$ and $\theta_f=50^\circ$, and (c) $\theta_i=30^\circ$ and $\theta_f=80^\circ$. The solid curves are calculations with $\mu=0.56$ and $D=35$ meV, the dash-dotted curves are the trapping-desorption fractions, and the dotted curves are the Knudsen distribution.

significant direct-scattering component. However the value of $\mu=0.56$ is chosen as a consequence of comparisons with the higher-energy data discussed below, where the much more pronounced direct-scattering component is extremely sensitive to μ . In this example the data do not exhibit a double-peaked structure and the calculated most probable energy (peak position) has a TOF corresponding to $E_f=12.57$ meV, very close to the equilibrium value of 11.6 meV at this temperature, again indicating that the scattering is mostly trapping-desorption.

Three calculated curves are shown in Fig. 11. The solid curve is the total differential reflection coefficient converted to TOF, and the dashed curve is the trapping-desorption contribution only. For comparison a Knudsen equilibrium distribution is included as a dash-dotted curve. The Knudsen distribution and the calculation are both normalized to unit intensity as in Eq. (1). Although it is apparent that the Knudsen curve, if renormalized to fit as closely as possible to the data, would match essentially as well as the total calculated intensity, the fact that it is smaller and nearly the same as the calculated trapping-desorption fraction indicates that there is significant direct scattering but its most probable energy and width is nearly the same as the equilibrium distribution. Because of the strong overlap of the direct and trapping-desorption fractions, it is not surprising that the data of Fig. 11 can be matched roughly as well by a total scattering intensity using a range of well depths from 20 meV to somewhat over 35 meV. We have chosen $D=35$ meV because of the much stronger constraints placed on this parameter by the higher-energy data considered below.

Three examples of data measured at the intermediate energy of 365 meV are shown in Fig. 12 at the same temperature of 135 K and for three different combinations of incident and final angles. The middle panel for $\theta_f=50^\circ$ and $\theta_i=30^\circ$, relatively close to normal incidence, does not exhibit a double-peaked structure. The other two panels, for $\theta_i=45^\circ$

and $\theta_f=50^\circ$ (upper panel) and $\theta_i=30^\circ$ and $\theta_f=80^\circ$ (lower panel), present a clear distinction between the rather sharp peak at short TOF and a broader shoulder at larger times. These data were taken from the middle panel of Fig. 2 and the lower two panels of Fig. 4, respectively, of Ref. 6. The solid curves in Fig. 12 are calculations carried out with $\mu=0.56$ and $D=35$ meV. The calculations explain the data quite well, and they show clearly the separation between the direct and trapping-desorption fractions. The value $D=35$ meV agrees well with that of the potential-energy function for this system developed in Ref. 6 in that it lies closer to the value of 33 meV that Gibson *et al.*⁶ obtained for the on-top position as opposed to their hollow-site value of 67 meV.

Also shown in Fig. 12 are the calculated trapping-desorption fraction and the Knudsen curves. Interestingly, the trapping-desorption fraction itself has a multiple-peaked structure with a small subpeak appearing at almost the same final energy as the direct-scattering contribution. This small high-energy subpeak comes from the first few collisions as the initially adsorbed particles travel in the potential well. These first few collisions have a high probability of ejecting particles back into the continuum with relatively little loss of energy compared to the direct-scattering fraction. However, it is clear that a significant part of the trapping-desorption fraction resembles closely the shape of the Knudsen curve, particularly in the low-energy tail.

It also becomes apparent from Fig. 12 that there is a straightforward manner in which the comparison of calculations with data allows for the determination of the two parameters. The effective mass determines the most probable final energy of the direct contribution and then the well depth determines the relative intensity of the trapping-desorption fraction which becomes bigger with increasing D . The peak position of the direct-scattering contribution is extremely sensitive to the mass ratio. This is why we chose the value $\mu=0.56$ as opposed to the value $\mu=0.62$ of Ref. 6 which was based on the Baule equations describing hard sphere scattering.

Three examples of data for scattering at the high energy $E_i=582$ meV, all of which exhibit the double-peaked structure, are shown in Fig. 13. The data were taken from the lower panel of Fig. 2 and the middle and lower panel of Fig. 3, respectively, of Ref. 6. The upper panel of Fig. 13 is for $\theta_i=45^\circ$ and $\theta_f=50^\circ$, the middle panel is for $\theta_i=45^\circ$ and $\theta_f=40^\circ$, and the lower panel is for $\theta_i=60^\circ$ and $\theta_f=40^\circ$.

In the upper two panels with $\theta_i=45^\circ$ two curves showing the total scattering intensity are shown, for $D=35$ and 45 meV, while in the lower panel with $\theta_i=60^\circ$ only the $D=35$ meV calculation is shown. All calculations were done with $\mu=0.56$, the value that leads to agreement with the data for the direct-scattering peak. The dotted curve is the Knudsen distribution and the dash-dotted curves show the trapping-desorption fraction for the calculation that is in best agreement with experiment.

It is interesting that at this larger incident energy the two cases with the more normal incident angle of 45° require a well depth of 45 meV in order to obtain agreement between calculations and data, while for the much more grazing incidence of 60° the best well depth is 35 meV, the same as used

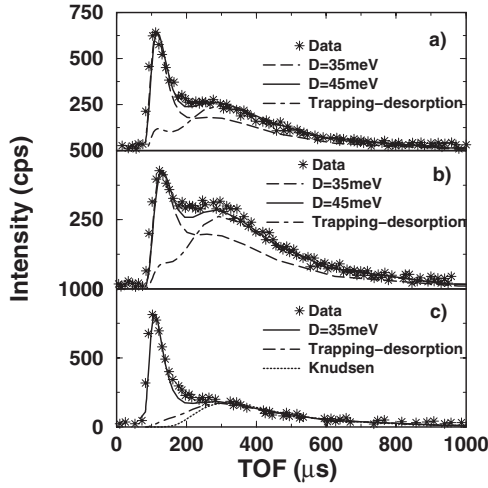


FIG. 13. Intensity versus TOF for Ar scattering from a 1-decanethiol layer on Au(111) with $E_i=582$ meV: (a) $\theta_i=45^\circ$ and $\theta_f=50^\circ$, (b) $\theta_i=45^\circ$ and $\theta_f=40^\circ$, and (c) $\theta_i=60^\circ$ and $\theta_f=40^\circ$. The curves are labeled similarly to those in Fig. 12 except calculations are shown for both $D=35$ and 45 meV in panels (a) and (b).

for all the lower-energy calculations. This appears to indicate that for larger normal incident energy the incoming atoms are probing deeper parts of the potential-energy landscape. Again, as in Fig. 12 the trapping-desorption fraction exhibits structure at larger final energies near the energy of the direct scattering.

Comparison of the present calculations to this Ar scattering data leads to a few general comments that can be applied to the observed energy-resolved spectra for cases in which a double structure appears due to the distinct phenomena of direct scattering and trapping-desorption:

(1) A characteristic double-feature structure, with a well-defined direct-scattering peak and a secondary peak or shoulder arising from trapping-desorption, appears only at relatively high incident-beam energy and when one or the other of θ_i or θ_f is large, as was already clear from Ref. 6. It is also necessary that the physisorption well depth is sufficiently large to cause significant trapping in the bound states during the initial collision, and the temperature must be smaller than D . However, for near-normal-incidence conditions and with a large well, the initial trapping becomes so large that the direct-scattering contribution becomes small. This explains the need for the incident angle to be relatively large in order to observe a double-peaked structure in the TOF intensities. This situation becomes evident in Fig. 14, which shows calculations for $E_i=582$ meV with $\theta_i=\theta_f=10^\circ$ and $D=35$ meV. Even though the incident energy is large compared to the well depth, the normal-incidence conditions gives rise to such large trapping that the total scattering is not very different from the trapping-desorption fraction.

(2) When the direct-scattering contribution is significant, the trapping-desorption intensity deviates substantially from that of an equilibrium Knudsen distribution. In fact, the trapping-desorption signal can exhibit structure and small peaklike features at high energies close to those of the direct contribution as shown in Figs. 12 and 13. However, in many cases the largest portion of the trapping-desorption intensity

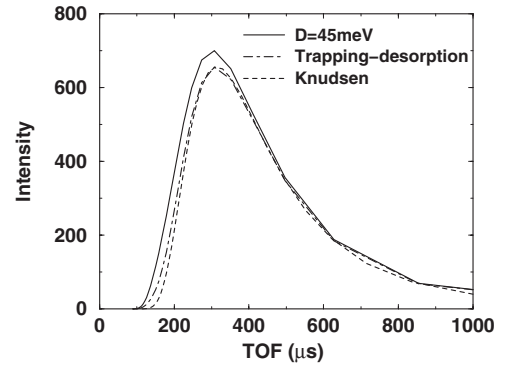


FIG. 14. Calculations similar to those of Fig. 13 with $E_i=582$ meV and $D=35$ meV but with $\theta_i=10^\circ$ and $\theta_f=10^\circ$, showing that for normal incidence a distinct direct-scattering peak is not expected.

resembles the shape of a Knudsen distribution. This is especially true for the low-energy tail.

(3) It is interesting to note that the direct and trapping-desorption fractions should have very characteristic and quite different signature behaviors in their temperature dependence. The direct scattering, which in the present calculations arises from a single collision with the surface, is essentially given by Eq. (18). Under conditions for which the direct scattering of Eq. (18) appears nearly Gaussian type in the energy transfer, which is the situation in several of the cases shown here, the mean-square energy deviation which is proportional to the full width at half maximum (FWHM) is^{11,12,42}

$$\langle E_f^2 \rangle = \frac{\text{FWHM}}{8 \ln(2)} = 2g(\mu, \theta)E_i k_B T_S, \quad (23)$$

where

$$g(\mu, \theta) = \frac{\mu[1 + f(\mu, \theta) - 2\sqrt{f(\mu, \theta)\cos\theta}]}{\left(1 + \mu - \frac{\mu \cos\theta}{\sqrt{f(\mu, \theta)}}\right)^2}, \quad (24)$$

with

$$f(\mu, \theta) = \left(\frac{\sqrt{1 - \mu^2 \sin^2\theta} + \mu \cos\theta}{1 + \mu}\right)^2, \quad (25)$$

where θ is the total scattering angle (i.e., the angle between \mathbf{p}_i and \mathbf{p}_f) and Eqs. (23)–(25) are obtained under the assumption of binary collision conditions for which $\bar{E}_f=f(\mu, \theta)E_i$. Thus, Eq. (23) shows that the FWHM of the direct-scattering peak will be approximately proportional to $\sqrt{T_S}$, which is the characteristic of the multiphonon-scattering regime. However, the trapping-desorption fraction will have a FWHM temperature dependence more closely approximating the linear in T_S behavior of the Knudsen distribution of Eq. (22). Similarly, the most probable intensity (maximum peak intensity) of the direct scattering will vary as $1/\sqrt{T_S}$ according to Eq. (18), while the trapping-desorption peak intensity should behave more like that of the $1/T_S$ behavior of the Knudsen distribution of Eq. (22).

(4) Finally, the comparison of the present calculations with the data provides a simple way to extract the two relevant parameters. The position in final energy of the narrow direct-scattering peak determines the value of the effective surface mass. In fact, the most probable energy is quite sensitive to this parameter. The intensity of the broad trapping-desorption peak increases with the well depth, and fixing the relative intensities of the two contributions determines D . This indicates that for the large incident energies considered here, the primary influence of the well depth is to establish the initial trapping fraction. Once trapped, the details of the shape of the potential well are not important as is evidenced by the fact that the long-time tail trapping-desorption fraction (the low-energy tail) eventually desorbs at thermal energies.

V. CONCLUSIONS

In this paper we have developed a theoretical formulation of the scattering of atomic projectiles with surfaces that includes not only the direct scattering arising from a single or a small number of collisions with the surface but also allows for trapping and subsequent collisions of trapped particles inside the physisorption well. The trapped particles can be followed until they eventually all desorb and leave the surface region. The multiple collisions of the initially trapped fraction with the surface are treated with an iteration algorithm that tracks trapped particles with both negative and positive total energies and determines at each subsequent collision the fraction scattered back into the positive-energy continuum which then leaves the surface region.

Using this theoretical formalism, first we have calculated numerous examples, in order to establish the conditions under which the trapped and subsequently desorbed particles approach an equilibrium distribution, i.e., to establish the conditions under which the Maxwell assumption is valid. Second we have used the theory to produce quantitative agreement with recent measurements, thus providing explanations of the basic underlying processes that give rise to the experimental scattered spectra.

Under many conditions, the observed spectra in gas-surface scattering experiments consist of two distinct contributions. The first contribution is the direct-scattering part, which is usually a relatively sharp peak with a most probable energy somewhat lower than the incident energy provided that the surface temperature is not large compared to the incident energy. The second of these contributions is the trapping-desorption, attributed to particles that are initially trapped and then spend a large time moving in the physisorption well where they slowly begin to exchange energy with the surface and then eventually desorb in a distribution at thermal energies corresponding to the surface temperature. A large part of the work considered here is devoted to determining when the trapping-desorption fraction approaches an equilibrium Knudsen flux.

Our calculations show that under conditions in which a clear direct-scattering and trapping-desorption double-peaked structure is evident in the energy-resolved spectra, the trapping-desorption fraction, although mainly emitted at

thermal energies, can differ considerably from an equilibrium distribution. It can even exhibit structure consisting of small peaks at high energy near the most probable energy of the direct scattered intensity. These higher-energy peaks arise from the first few collisions with the surface inside the well, indicating that these initial collisions have a large probability of ejecting particles into the continuum with little additional energy loss as compared to the direct scattering. However, even under conditions for which the trapping-desorption fraction is highly nonequilibrium, its low-energy tail still is well described by a Knudsen distribution. Thus, our calculations show that the Maxwell assumption is rarely achieved in real experimental conditions, although it is very useful as an approximate guide as evident from the fact that it is still often used as a method to analyze measured data.

We carried out a number of calculations in order to characterize the conditions under which the trapping-desorption fraction does approach an equilibrium distribution. Basically, equilibrium behavior is achieved only for cases where the direct scattering is negligible and average trapping times are long, which implies that nearly all of the incident beam is adsorbed after the first collision. This implies an incident energy relatively small compared to the interaction potential physisorption well depth and temperatures corresponding to energies (measured in units of $k_B T_S$) that are also small compared to the well depth. The approach to equilibrium occurs more rapidly with larger gas-to-surface-atom mass ratios when this ratio is less than unity.

The approach to equilibrium of the trapping-desorption fraction was studied as a function of all the initial experimental parameters that can be manipulated, including the projectile and surface mass, the well depth of the potential, the incident energy and angles, the final scattering angles, and the surface temperature. For example, as the well depth is increased with all other parameters held constant, we find that the energy-resolved scattered spectrum rather quickly approaches that of a Knudsen distribution when the well depth becomes significantly larger than the incident energy provided the temperature is also small compared to the well depth. The angular behavior becomes independent of azimuthal angle under the same conditions that the energy distribution becomes Knudsen type. However, the polar angle $\cos \theta_f$ behavior is only approximately obeyed for conditions under which the energy dependence first approaches equilibrium, even though the energy dependence is nearly Knudsen type at all polar angles. Only for well depths very large compared to the incident energy and temperature does the trapping-desorption fraction achieve the classic Knudsen $\cos \theta_f$ shape.

The rapid approach toward azimuthal angle independence of the calculated trapping-desorption fraction is easily understood in the context of our calculations because of the significant amount of large-angle scattering caused by the binary collision differential reflection coefficient of our Eq. (18) used for all multiple-scattering collisions. After just a few collisions, this rapidly causes the trapped atoms to lose memory of their incident azimuthal angle. The slow approach of the trapping-desorption fraction toward the Knudsen $\cos \theta_f$ distribution in polar angles, even for cases in which the energy distribution quickly achieves the expected

Knudsen behavior, is less easy to explain and not completely understood.

In this formalism, because of its iterative approach, the number of collisions of the trapped particles with the surface can be followed. This means that trapping times can be calculated as well as other information such as the relative fractions of particles trapped with negative total energies and those trapped in the chattering states having positive total energies. Under conditions in which the trapping-desorption fraction did achieve near equilibrium, the trapping times were estimated to be as large as 10^{-8} – 10^{-7} s. The positive total-energy chattering fraction can be large under conditions where equilibrium is not achieved. But for conditions that produce equilibrium in the trapping-desorption, the fraction of trapped particles residing in the chattering states becomes negligible.

An important aspect of this work is that the theoretical model used for the calculations provides quantitative explanations of experimental measurements. We made comparisons with important and recent Ar scattering data obtained in beam-surface scattering experiments with a surface consisting of a self-assembled adsorbed layer of 1-decanethiol on a well-ordered Au(111) substrate.⁶ In agreement with the experimental observations, we found that clearly distinguishable direct and trapping-desorption contributions arise when the incident-beam energy is large compared to the potential-well depth and when one or the other of the incident and detector angles is large relative to the surface normal. In addition the calculations indicate that, in order to resolve distinct direct and trapping-desorption features, the temperature must be small compared to the well depth and the well depth must be large enough to cause trapping of a significant fraction of the incident beam at the initial collision.

Under conditions for which distinct direct and trapping-desorption features were evident, the data can be used to determine two important characteristics of the interaction potential, the effective surface mass of the adsorbate and the well depth. The effective mass is determined by matching the calculated direct-scattering peak to that of the experiment, and the well depth then is determined by matching the relative intensity of the trapping-desorption contribution. As discussed in Ref. 6 the calculated potential-well depth is not uniform but varies substantially across the surface unit cell. To obtain agreement with the experiments, our calculations require a larger well depth when the incident energy is large

and combined with near-normal incident angles. We interpret this as indicating that the shallower parts of the potential well are more strongly sampled with more grazing incident angles, while the deeper parts of the potential well are probed at higher energies and more normal incidence.

An interesting prediction coming out of this work is that the direct and trapping-desorption contributions have clearly different signature behaviors as a function of surface temperature. The FWHM of the direct peak should increase approximately with the square root of the temperature, whereas the trapping-desorption has a full width that increases approximately linearly with T_S , similarly to the Knudsen distribution. The most probable intensity of the direct peak, according to the scattering model used here, decreases inversely with the square root of temperature, while the trapping-desorption decreases roughly linearly with the inverse of the temperature, again similarly to the Knudsen distribution. For both peaks, the increase in FWHM and decrease in most probable intensity is the behavior expected in order to preserve unitarity. It should be noted that the direct scattering, as shown in the approximations to Eq. (18) appearing in Eqs. (23)–(25), exhibits the same behavior in the incident energy E_i as it does in the temperature T_S . However, the most appropriate parameter in which to carry out an experimental search for these behaviors would be the temperature because the interaction potential surface is likely to change with variation in E_i but is less likely to change with T_S .

This work demonstrates that calculations of direct scattering, trapping, and desorption in atom-surface scattering can provide real quantitative explanations of experiments as well as indicate the conditions for the validity of the Maxwell assumption on the equilibrium nature of the trapping-desorption fraction. It shows that the interaction potential model must contain two essential ingredients: a physisorption well depth and allowance for transfer of mechanical energy between the projectile and the surface atoms. However, it also shows that the most important aspect is to have a theory in which the statistical mechanics is treated in a reasonably correct manner.

ACKNOWLEDGMENT

This work was supported in part by the U.S. Department of Energy under Grant No. DE-FG02-98ER45704.

*jmanson@clemson.edu

¹J. C. Maxwell, *Philos. Trans. R. Soc. London* **170**, 231 (1879).

²M. Knudsen, *The Kinetic Theory of Gases*, 3rd ed. (Wiley, New York, 1950).

³J. E. Hurst, C. A. Becker, J. P. Cowin, K. C. Janda, L. Wharton, and D. J. Auerbach, *Phys. Rev. Lett.* **43**, 1175 (1979).

⁴J. E. Hurst, Jr., L. Wharton, K. C. Janda, and D. J. Auerbach, *J. Chem. Phys.* **83**, 1376 (1985).

⁵A. C. Kummel, G. O. Sitz, R. N. Zare, and J. C. Tully, *J. Chem. Phys.* **91**, 5793 (1989).

⁶K. D. Gibson, N. Isa, and S. J. Sibener, *J. Chem. Phys.* **119**, 13083 (2003).

⁷B. Scott Day, Shelby F. Shuler, Adonis Ducre, and John R. Morris, *J. Chem. Phys.* **119**, 8084 (2003).

⁸Guoqing Fan and J. R. Manson, *Phys. Rev. B* **72**, 085413 (2005).

⁹Guoqing Fan and J. R. Manson, *Phys. Rev. Lett.* **101**, 063202 (2008).

¹⁰R. Brako and D. M. Newns, *Phys. Rev. Lett.* **48**, 1859 (1982); *Surf. Sci.* **123**, 439 (1982).

- ¹¹Andre Muis and J. R. Manson, *Phys. Rev. B* **54**, 2205 (1996).
- ¹²A. Sjölander, *Ark. Fys.* **14**, 315 (1959).
- ¹³D. A. Micha, *J. Chem. Phys.* **74**, 2054 (1981).
- ¹⁴J. R. Manson, *Phys. Rev. B* **43**, 6924 (1991).
- ¹⁵J. R. Manson, V. Celli, and D. Himes, *Phys. Rev. B* **49**, 2782 (1994).
- ¹⁶W. H. Weinberg and R. P. Merrill, *J. Chem. Phys.* **56**, 2881 (1972).
- ¹⁷S. B. M. Bosio and W. L. Hase, *J. Chem. Phys.* **107**, 9677 (1997).
- ¹⁸M. A. Freedman, A. W. Rosenbaum, and S. J. Sibener, *Phys. Rev. B* **75**, 113410 (2007).
- ¹⁹D. J. Gaspar, A. T. Hanbicki, and S. J. Sibener, *J. Chem. Phys.* **109**, 6947 (1998).
- ²⁰J. E. Hurst, Lennard Wharton, K. C. Janda, and D. J. Auerbach, *J. Chem. Phys.* **78**, 1559 (1983).
- ²¹C. T. Rettner, D. S. Bethune, and D. J. Auerbach, *J. Chem. Phys.* **91**, 1942 (1989).
- ²²N. Lipkin, R. B. Gerber, N. Moiseyev, and G. M. Nathanson, *J. Chem. Phys.* **100**, 8408 (1994).
- ²³M. Manning, J. A. Morgan, D. J. Castro, and G. M. Nathanson, *J. Chem. Phys.* **119**, 12593 (2003).
- ²⁴J. A. Morgan and G. M. Nathanson, *J. Chem. Phys.* **114**, 1958 (2001).
- ²⁵W. R. Ronk, D. V. Kowalski, M. Manning, and G. M. Nathanson, *J. Chem. Phys.* **104**, 4842 (1996).
- ²⁶M. E. King, G. M. Nathanson, M. A. Hanning-Lee, and T. K. Minton, *Phys. Rev. Lett.* **70**, 1026 (1993).
- ²⁷N. Isa, K. D. Gibson, T. Yan, W. Hase, and S. J. Sibener, *J. Chem. Phys.* **120**, 2417 (2004).
- ²⁸F. Frenkel, J. Häer, W. Krieger, H. Walther, G. Ertl, J. Segner, and W. Vielhaber, *Chem. Phys. Lett.* **90**, 225 (1982).
- ²⁹A. Mödl, H. Robota, J. Segner, W. Vielhaber, M. C. Lin, and G. Ertl, *J. Chem. Phys.* **83**, 4800 (1985).
- ³⁰A. W. Kleyn, A. C. Luntz, and D. J. Auerbach, *Phys. Rev. Lett.* **47**, 1169 (1981).
- ³¹H. Mortensen, E. Jensen, L. Diekhöner, A. Baurichter, A. C. Luntz, and V. V. Perunin, *J. Chem. Phys.* **118**, 11200 (2003).
- ³²C. T. Rettner, F. Fabre, J. Kimman, and D. J. Auerbach, *Phys. Rev. Lett.* **55**, 1904 (1985).
- ³³Y. Huang, A. M. Wodtke, H. Hou, C. T. Rettner, and D. J. Auerbach, *Phys. Rev. Lett.* **84**, 2985 (2000).
- ³⁴A. E. Wiskerke and A. W. Kleyn, *J. Phys.: Condens. Matter* **7**, 5195 (1995).
- ³⁵J. B. C. Pettersson, G. Nyman, and L. Holmlid, *J. Chem. Phys.* **89**, 6963 (1988).
- ³⁶M. K. Ainsworth, V. Fiorin, M. R. S. McCoustra, and M. A. Chesters, *Surf. Sci.* **433-435**, 790 (1999).
- ³⁷C. T. Rettner, J. Kimman, F. Fabre, D. J. Auerbach, J. A. Barker, and J. C. Tully, *J. Vac. Sci. Technol. A* **5**, 508 (1987).
- ³⁸J. Segner, H. Robota, W. Vielhaber, G. Ertl, F. Frenkel, J. Häger, W. Krieger, and H. Walther, *Surf. Sci.* **131**, 273 (1983).
- ³⁹G. O. Sitz, A. C. Kummel, and R. N. Zare, *J. Chem. Phys.* **89**, 2558 (1988).
- ⁴⁰O. Weiße, C. Wesenberg, M. Binetti, E. Hasselbrink, C. Corriol, G. R. Darling, and S. Holloway, *J. Chem. Phys.* **118**, 8010 (2003).
- ⁴¹W. L. Hase, R. J. Duchovic, X. Hu, A. Komornicki, K. Lim, D.-h. Lu, G. H. Peslherbe, K. N. Swamy, S. R. Vande Linde, H. Wang, and R. J. Wolf, *QCPE* **16**, 671 (1996).
- ⁴²C. A. DiRubio, D. M. Goodstein, B. H. Cooper, and K. Burke, *Phys. Rev. Lett.* **73**, 2768 (1994).